SCIENCE CHINA
Information Sciences

• RESEARCH PAPER •
Special Topic: Two-Dimensional Materials and Device Applications

June 2023, Vol. 66 160405:1–160405:8
https://doi.org/10.1007/s11432-022-3719-4

Selective enriching of trionic emission in a WS_2-ZnO hybrid through type-II band alignment

Jin Feng LEONG[1], Kim Yong LIM[1], Xiao WU[2], Qinghua XU[2], Chorng Haur SOW[1] & Eng Tuan POH[1*]

[1]*Department of Physics, National University of Singapore, Singapore* 117551*, Singapore;*
[2]*Department of Chemistry, National University of Singapore, Singapore* 117543*, Singapore*

Received 30 November 2022/Revised 10 February 2023/Accepted 28 February 2023/Published online 10 May 2023

Abstract Strategies to modulate the exciton dynamics in ultrathin two-dimensional (2D) semiconductors have always been an integral component in the bid towards improved optoelectronics and quantum photonic devices. The capability to non-destructively tune the relaxation dynamics, valley polarization, binding energies, and population ratio of various excitonic species has been well-sought for advanced applications. Through the rationale design of a WS_2-ZnO hybrid platform, we present a distinct increment in the trion-to-exciton ratio for WS_2 emission across a patterned heterostructure. The shift in dominant excitonic species arose due to the efficient charge segregation at the spatially confined interface of the type-II heterostructure. Owing to the charge transfer process, the resultant emission profile presents up to four times amplification in the trion-to-exciton ratio, with temperature variable trion binding energies up to 59 meV. Since trions possess non-zero charge and spin degrees of freedom, the provision of a higher density of trions with increased binding stability would encourage new opportunities for reproducible optoelectronics and quantum emitters.

Keywords heterostructure, trions, type-II band alignment

Citation Leong J F, Lim K Y, Wu X, et al. Selective enriching of trionic emission in a WS_2-ZnO hybrid through type-II band alignment. Sci China Inf Sci, 2023, 66(6): 160405, https://doi.org/10.1007/s11432-022-3719-4

1 Introduction

The ability to manipulate the properties of exciton quasiparticles in semiconductor nanostructures remains highly desired in the technological advancement for efficient excitonic and quantum devices [1, 2]. Owing to strong light-matter interaction, excitonic nanomaterials typically present rich exciton-optical properties that can be exploited for a variety of optoelectronics (phototransistors [3], light-emitting diodes [4], photonic memory [5]), valleytronics [6], quantum computing [7, 8], and lasing applications [9]. Of the various classes of excitonic nanomaterials, 2D monolayers of transition metal dichalcogenides (TMDs) stands out due to their ultrathin feature. With quantum confinement and reduced dielectric screening arising from the decreased z-dimensions, these monolayer TMDs (e.g., WS_2, MoS_2, WSe_2, $MoSe_2$) present much stronger exciton binding energies (∼0.2–0.4 eV) [10–12] in comparison to conventional III-V excitonic semiconductors (< 7 meV). As such, the TMDs feature a broad family of stable free and bound excitons (neutral excitons, trions, biexcitons, defect-bound excitons) [13] of similarly high binding energies that recombine radiatively at room temperature.

Theoretically, trions are expected to carry more information than electrons and excitons for electronic and quantum applications [14]. However, given the relatively lower binding energy of trions (tens of meV) as compared to excitons (hundreds of meV), the stability of trions is inherently compromised. Furthermore, under the thermal influence, a strong many-body correlation that scatters from bright to dark trionic states reduces the quantity of optically permissible trionic transitions [15]. Over the years, many strategies have been proposed to provide effective handles at tuning trion binding energies and trion-to-exciton ratios, through photodoping strategies [16, 17] and modulations in orbital angular

* Corresponding author (email: phyetp@nus.edu.sg)

momentum [18], and power density [19] of the excitation light source. However, such processes typically provide in situ trion enhancement only, requiring consistent light irradiation to sustain the process. The possibility of the slightest damage and change accorded to the sample upon prolonged or high energy irradiation is expected to easily invoke inconsistencies and variations between measurement runs. On the contrary, the use of heterostructure geometries to generate charge transfer dynamics at the material interface allows for permanent, stable, and non-destructive alterations to the exciton properties. With careful selection of the nanomaterial variants and the associated relative work functions, the charge transfer process can be flexibly refined through the designed band alignment to achieve the desired heterojunctions.

Herein, we demonstrate the capability to influence the trion-to-exciton ratio in an exfoliated tungsten disulfide (WS_2) monolayer overlaid atop a patterned zinc oxide (ZnO) thin film. The type-II band alignment at the interface encourages efficient charge separation and charge transfer to yield excess electrons at the WS_2 monolayer. As a result, the trion-to-exciton ratio was improved up to four times with trion binding energies on the order of 50 meV. Across samples, the high reproducibility and measurement repeatability ensures enhanced stability that is desirable for subsequent advanced optoelectronic and quantum applications. With the stable excitonic emissions (in the visible range) of ultrathin WS_2 modulated by the wide band gap ZnO film at zero optical crosstalk, the resultant heterostructure presents ideal optical tuning appropriate for the various applications above. In comparison with other substrates across previous reports exploring similar heterostructure geometries, ZnO outperforms in its role as a trion enhancer for WS_2 monolayers (Table S1).

2 Experimental section

2.1 Physical instrumentations

Optical and fluorescence images of the samples were captured using the Olympus BX51 microscope, coupled with an Olympus U-HGLGPS mercury lamp and a set of dichroic filters. The Raman and photoluminescence (PL) spectra were obtained using a Renishaw inVia 2000 Micro-Raman spectrometer, while the Raman and PL maps were obtained with a WiTec Alpha 300 R confocal Raman microscope. For low temperature PL measurements, the spectrometer was coupled with a Linkam THMS 600 temperature-controlled stage under liquid nitrogen flow. The atomic force microscopy (AFM) and kelvin probe force microscopy (KPFM) results were acquired from a Bruker Dimension® Icon^{TM} AFM, detailing the sample's topographical profile and work function distribution.

2.2 Sample preparation

ZnO fingers were patterned by lithography involving direct laser writing upon a spin-coated photoresist film prior to ZnO thin film sputtering using a Denton Vacuum Discovery^{TM} 18 RF Sputtering Deposition System. The sample was prepared separately upon SiO_2/Si and doped-Si substrates for the respective optical and KPFM characterizations. Upon these substrates, 23 nm of ZnO thin films were sputtered by exposing the target to 130 W RF for 180 s amidst vacuum conditions of 8×10^{-6} Torr. WS_2 monolayers were mechanically exfoliated using blue Nitto tapes (Nitto Denko Co., SPV 224P) from a bulk crystal purchased from HQ Graphene and transferred with the aid of a polydimethylsiloxane (PDMS) film onto the ZnO fingers. The patterned morphology allows simultaneous access to WS_2 on ZnO and WS_2 on the substrate (SiO_2/Si) regions in close proximities for the various characterizations.

3 Results and discussion

The schematic in Figure 1(a) outlines the overall phenomenon intended from the designed heterostructure geometry. With the exfoliated WS_2 monolayer transferred upon the sample region spanning both the patterned ZnO fingers and the underlying SiO_2 substrate, the PL of the monolayer (under 532 nm excitation) from these regions can be differentiated. Of which, the WS_2 on the ZnO region is expected to present a greater extent of trion contribution as compared to the pristine (WS_2 on SiO_2 reference) region. Figures 1(b) and (c) display the respective optical and fluorescence images of the as-prepared heterostructure. Under the broad detector range of the microscope charged-coupled device (CCD) camera, with the selected dichroic filter cube (λ_{ex} (narrow pass) = 500–560 nm; λ_{em} (long pass) $\geqslant$ 590 nm), the

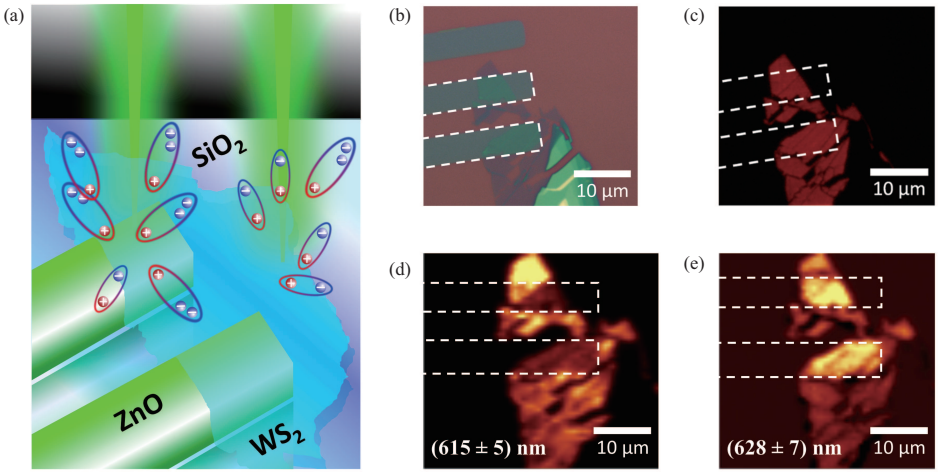

Figure 1 (Color online) Design and characterization of WS_2-ZnO heterostructure. (a) Schematic illustration of heterostructure design and intended optical phenomenon. Emplaced over differentiation regions comprising the SiO_2 substrate and ZnO fingers, the WS_2 monolayer is optically influenced by the underlying component – the monolayer region atop SiO_2 presents an exciton dominant emission, whereas the region atop the ZnO fingers is modified to emit with a greater trion ratio. (b) Optical micrograph showing the WS_2-ZnO heterostructure assembled from transferring an exfoliated WS_2 monolayer onto the ZnO fingers, along with the corresponding (c) fluorescence image and (d), (e) PL maps over the whole sample region. (d) The congruent PL map was established over the exciton emission range at (615 ± 5) nm. (e) The identical PL map was readjusted to show emission over the trion range at (628 ± 7) nm. The exact locations of the underlying ZnO fingers are marked out by the white dashed rectangles in (b)–(e).

monolayer fluorescence is presented as an averaged uniform emission, undifferentiated in its excitonic species. Nonetheless, the uniform emission assures the sample as a monolayer with consistent quality. With greater scrutiny under the PL mapping, Figures 1(d) and (e) represent the sample PL with stronger distinction of its regions atop the ZnO fingers and SiO_2 substrate. Within the wavelength range for neutral excitons (Figure 1(d), (615 ± 5) nm), the region of WS_2 on the ZnO fingers displayed an obvious intensity reduction against the peripheral WS_2 on the SiO_2 region. Comparatively, the PL map in the range of (628 ± 7) nm presented an inverse distribution, with enhanced trion intensity for WS_2 on ZnO in compensation for its reduced exciton contributions. Together, the PL maps over the exciton and trion emission wavelengths distinctly revealed the enhanced trion-to-exciton ratio for WS_2 emplaced atop the ZnO fingers.

To quantify the extent of trion increase relative to the exciton count, single spot PL spectra were acquired at the different sample regions and deconvoluted by separate Gaussian fits for the trions and excitons. The spectrum obtained from the pristine (WS_2 on SiO_2) domain (Figure 2(a), marked spot: red "x") displayed clear exciton dominance (Figure 2(b)) with the ratio (exciton-to-trion) quantifier $\frac{I_{X^-}}{I_{X^0}}$ of 0.53, where I_{X^-} and I_{X^0} refer to the intensities of the trion and exciton emissions respectively. In contrast, the spectrum acquired of the heterostructure (WS_2 on ZnO) (Figure 2(c), marked spot: yellow "x") demonstrated the inverse – trion dominance (Figure 2(d)) coherent with the PL mapping results, giving an $\frac{I_{X^-}}{I_{X^0}}$ ratio of 2.21. These results present an optimal four times increment in the ratio metric. Herein, it is possible that an efficient conversion of excitons to trions may have occurred, due to the influx of charge carriers into the WS_2 monolayer under the electropotential influence across the heterojunction. In the presence of excess free carriers, the consumption of excitons to form a near equivalence of trions through the relation $X^0 + e^- \rightarrow X^-$ prompted the increment factor of four.

Across different sample trials (Figures S1 and S2), the same set of characterization techniques imposed upon the exfoliated WS_2 monolayers presented coherent results – the monolayer segment emplaced upon the ZnO fingers would always present increased trion intensities in compensation for exciton decline. The enhancement in the trion-to-exciton ratio was highly reproducible across the various samples, regardless of the shape, size or even fracture densities in the exfoliated WS_2 flakes. Interestingly, the concomitant Raman mapping (Figure S3) of the exfoliated monolayer also revealed distinct intensity contrast across the differing substrate regions (SiO_2 and ZnO). The maps acquired over the wavenumber ranges associated with the in-plane E^1_{2g} (350 ± 1) cm^{-1} (Figure S3(a)) and out-of-plane A_{1g} (417 ± 3.5) cm^{-1} (Figure S3(b)) phonon modes both exhibit attenuated intensities at the WS_2 on ZnO domains as opposed to the peripheral WS_2 on SiO_2 regions. Under closer scrutiny through spectra comparison (Figures S3(c)–(e)),

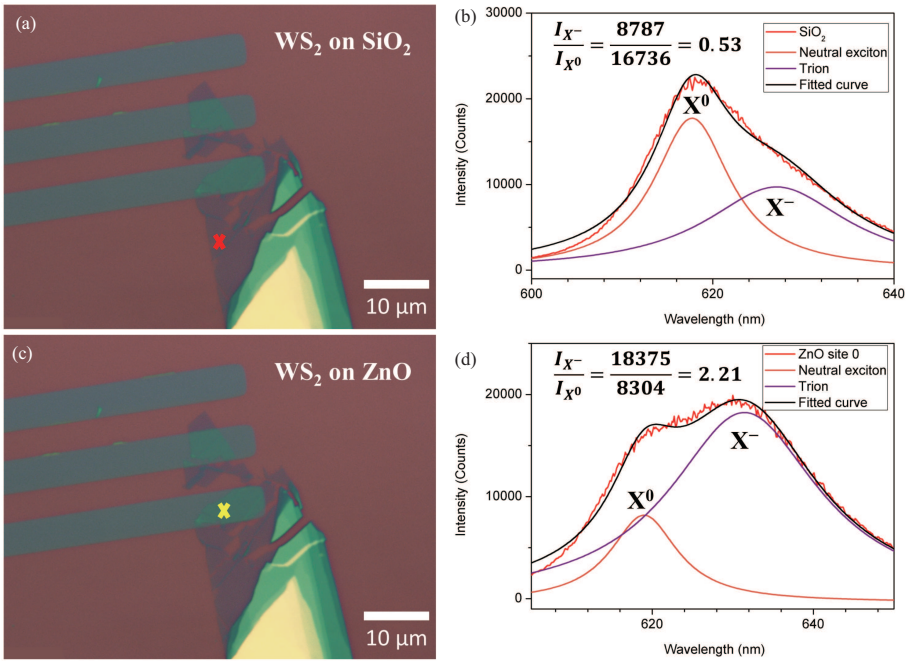

Figure 2 (Color online) PL spectroscopy of WS_2-ZnO heterostructure. (a) Microscope image of the WS_2-ZnO heterostructure, marking out (in red "x") the location where the single spot PL spectrum was acquired for the WS_2 on SiO_2 reference. (b) The corresponding PL spectrum (under 532 nm excitation) for the spot marked in (a), deconvoluted of the exciton (X^0) and trion (X^-) peak contributions. The associated metric – trion-to-exciton intensity ratio adopts a value of 0.53. (c) Microscope image of the WS_2-ZnO heterostructure, marking out (in yellow "x") the location where the single spot PL spectrum was acquired for the WS_2 on the ZnO domain. (d) The corresponding PL spectrum (under 532 nm excitation) for the spot marked in (c), similarly deconvolved into its exciton (X^0) and trion (X^-) peak contributions. The associated metric – trion-to-exciton intensity ratio is enhanced up to 2.21.

the peaks relating to the vibrational modes were found to adopt similar decline of approximately 37% in intensity. This marks evidence on the direct contact of the WS_2 monolayer upon the ZnO fingers, in which the effective anchoring of the monolayer upon the rigid ZnO layer suppressed WS_2 vibration across both the x- and y-planes.

To understand the energetics associated with the formation of the heterojunction, a separate replica of the heterostructure was constructed on a doped-silicon (Si) substrate for KPFM characterization. Figure 3(a) presents the crafted heterostructure, with the monolayer segment of the exfoliated WS_2 sample outlined by the white dashed polygon. Transferred onto the pre-patterned ZnO finger (outlined by the yellow dashed rectangle), a slight optical contrast was discernible at the intersection of the two domains where the heterojunction was established. Under fluorescence imaging, the monolayer emits the characteristic red emission with distinctly enhanced intensity over the heterostructure region in the corresponding Figure 3(b). Zoomed in under the AFM characterization in Figure 3(c), the heterostructure domain was marked out with different topographical features for the respective regions. The ultrathin monolayer was identifiable by the clear kinked edges, along with slight amounts of fractures and folds incurred during the transfer process, giving a visibly different surface profile when blanketed over the rougher sputtered ZnO surface. With the marked boundaries and distinct surface features, the different sample zones were conveniently identified for comparison in the complementary KPFM interleave mapping (Figure 3(d)). Of which, the three zones of WS_2 on Si, WS_2 on ZnO, and ZnO on Si were determined to adopt respective surface potentials/contact potential difference (CPD) of 0.0171, 0.0456, and −0.2770 eV relative to the tip potential (Figure S4). With a constant tip potential and the common Si substrate base as reference, the relative difference in Fermi level (E_F) between WS_2 and ZnO can be calculated to give 0.2941 eV through the difference in surface potential between WS_2 on Si and ZnO on Si.

With the relative Fermi level between WS_2 and ZnO quantified, the construction of a band alignment model would proceed to explain the fundamentals associated with the trion enhancement phenomena. As illustrated in Figure 4, the initial states of WS_2 and ZnO energy bands, when aligned with reference to Anderson's rule, manifest as a staggered gap that indicates a type-II band heterostructure upon contact. As the heterostructure forms, the band renormalization lines up the respective Fermi levels, resulting in an

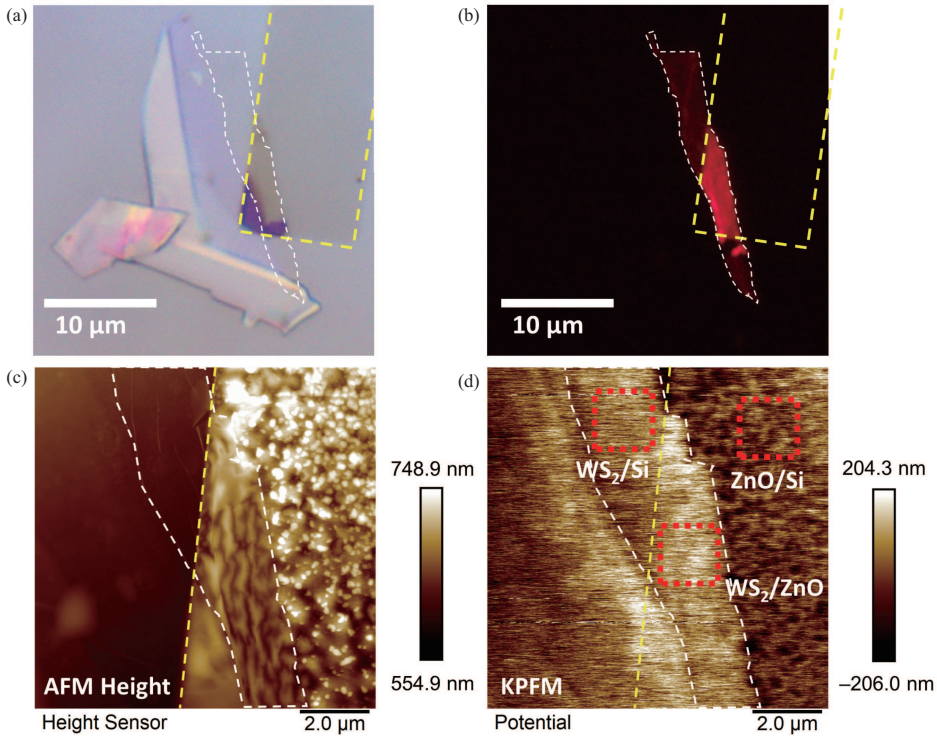

Figure 3 (Color online) KPFM measurement for WS_2-ZnO heterostructure. (a) Optical micrograph of the WS_2-ZnO heterostructure constructed. The monolayer segment of the exfoliated flake is demarcated by the white dashed line, and positioned on top of the ZnO finger marked by the yellow dashed rectangle. The heterojunction is established at the intersection of these yellow and white dashed domains. (b) Corresponding fluorescence image of the WS_2-ZnO heterostructure. Similarly, the monolayer and ZnO regions are marked out by the same set of dashed boundaries. Distinct red fluorescence was observed across the monolayer sample, with enhanced emission over the overlaid heterojunction domain. (c) AFM topographical landscape across the heterojunction area, detailing the various domains of multilayer WS_2, monolayer WS_2 on Si, WS_2 on ZnO heterojunction, and ZnO finger, in corresponding reference for the KPFM map in (d). The white dashed line marks out the WS_2 monolayer region while the yellow dashed line outlines the ZnO boundary on the right. (d) KPFM characterization for the WS_2-ZnO heterostructure was established, demonstrating the variance in surface potential across the various demarcated domains. The white dashed line marks out the WS_2 monolayer region while the yellow dashed line outlines the ZnO finger on the right. The red spotted squares denote the regions where the averaged surface potential was quantified to reveal the relative work function of the WS_2 and ZnO components.

electropotential built-up at the interface that promotes charge segregation into the respective components (e^- towards WS_2, h^+ towards ZnO) [20,21]. As the overall Fermi level shifts upwards, the population of electrons in the conduction band increases, favouring the formation of negative trions in the WS_2 sample. In contrast, similar effects were not observed for WS_2/SiO_2 interfaces due to a large difference between the energy bands between WS_2 and SiO_2.

Under scrutiny from the temperature variable PL instrumentation, the temperature dependent stability of the trions was further assessed. Figures 5(a) and (b) show the progression of WS_2 PL with decreasing temperatures for the WS_2 on SiO_2 and WS_2 on ZnO samples respectively. From 323.15 down to 77.15 K, the peak separation between the exciton and trion feature enlarges (Figure 6), along with distinct peak blue shifts and increasing trion weightage. The trion binding energy (B.E.) was effectively derived from the difference in the energies between the trion and neutral exciton, in accordance with the following relation:

$$\text{B.E.}(X^-) = \text{Energy}(X^0) - \text{Energy}(X^-),$$

where X^0 refers to the neutral exciton and X^- refers to the trion.

At room temperature, the standard reference of pristine WS_2 on SiO_2 substrate presents a trion binding energy of 38 meV, in agreement with previous literature reports [22–24], whilst that for the WS_2 on ZnO heterostructure was marginally elevated to 43 meV. With decreasing temperatures, the influence of thermal fluctuations on the stability of the trions is weakened, and trions are less likely to dissociate into neutral excitons and electrons. The associated trion binding energies increase to an optimal 41 and 59 meV for the WS_2 samples on SiO_2 and ZnO, respectively. Herein, it is critical to note that the enhancement in trion binding energy brought about by the ZnO substrate (43 meV at 298.15 K) surpasses all values for WS_2 on SiO_2 across the whole temperature range (30 to 41 meV

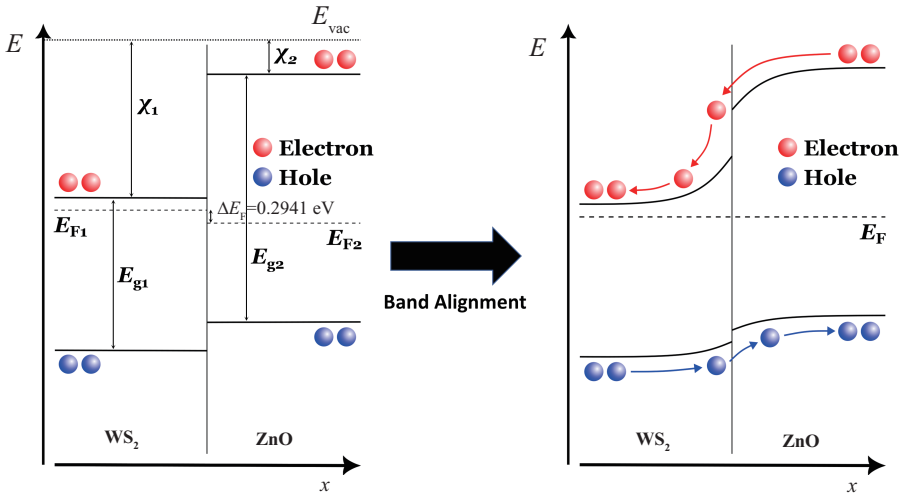

Figure 4 (Color online) Hypothesized band alignment model for charge dynamics across the WS_2-ZnO heterointerface. Initial relative band position of WS_2 and ZnO prior to contact, aligned in accordance with Anderson's rule. Upon direct contact to establish the heterojunction, the band renormalization with aligned Fermi level results in the type-II heterostructure with the associated charge gradient. Under the influence of the local electropotential at the interface, the charge potential drives high electron density toward the WS_2 domain, while holes migrate into the ZnO region. The resultant charge imbalance confers an increased probability for negative trion binding in place of neutral excitons, as reflected in the resultant PL acquired. The label E_{vac} refers to the vacuum level, while E_F, χ, and E_g refer to the Fermi level, electron affinity, and band gap of the materials, respectively.

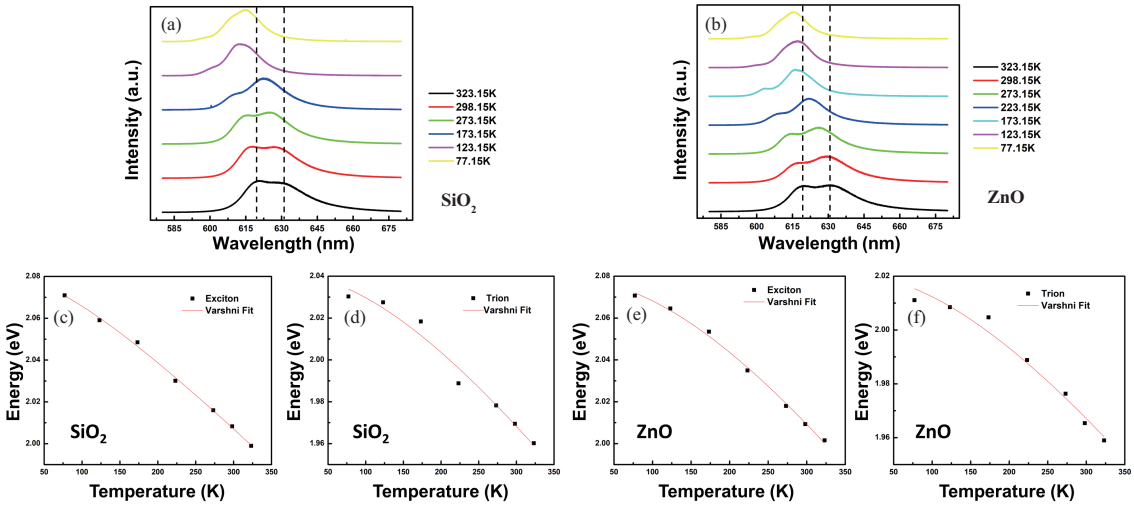

Figure 5 (Color online) Low temperature PL characteristics for WS_2 emission on pristine SiO_2 and ZnO substrate. (a) Evolution of PL spectra for WS_2 on SiO_2 from 323.15 down to 77 K. Dashed black lines mark as reference for initial peak positions of exciton and trion at 323.15 K. (b) Evolution of PL spectra for WS_2 on ZnO from 323.15 down to 77 K. Dashed black lines mark as reference for initial peak positions for exciton and trion at 323.15 K. Trends of (c) exciton and (d) trion energies under temperature variation, fitted under the Varshni relation. Trends of (e) exciton and (f) trion energies under temperature variation, fitted under the Varshni relation.

between 325.15 and 77.15 K). This reiterates the superior effect brought about by the ZnO substrate, with the potential for further enhancement at low temperatures (up to 59 meV at 77.15 K). With reduced dielectric screening in the ultrathin WS_2 monolayers, the electric field between the charges that form the excitons and trions significantly extends beyond the 2D material plane and thus, becomes substantially affected by the work function and dielectric constant of the underlying SiO_2 (κ = 3.7–3.9) and ZnO (κ = 8.2–9.3) layers [25]. Under such conditions, the resultant band renormalization across the WS_2-ZnO heterostructure interface effectively augmented the trion binding energy through enhanced dielectric screening by the ZnO underlayer.

The temperature dependent blue-shift for both excitons and trions from the instances involving the SiO_2 and ZnO substrates were subsequently modeled using the Varshni relation (Figures 5(c)–(f)) [26].

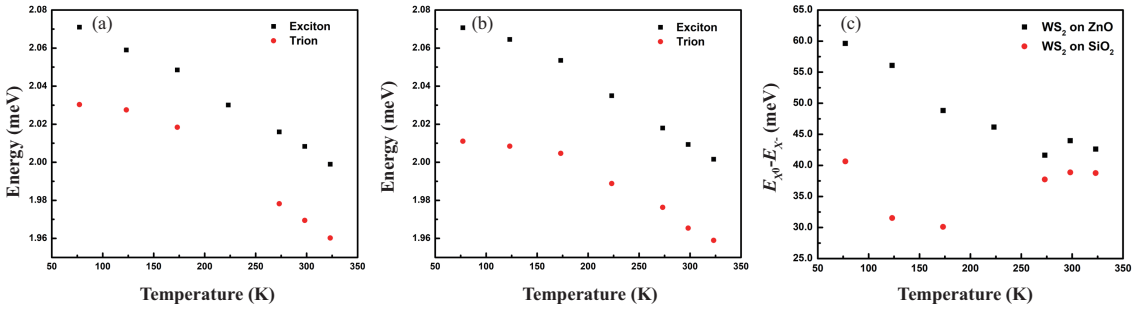

Figure 6 (Color online) Temperature dependent trends in exciton and trion energies for WS_2-SiO_2 and WS_2-ZnO comparison. (a) Trending increase of exciton and trion energies for WS_2 on SiO_2 under decreasing temperature conditions. (b) Trending increase of exciton and trion energies for WS_2 on ZnO heterostructure under decreasing temperature conditions. (c) Temperature variable shifts in trion binding energy for WS_2 on SiO_2 compared against WS_2 on ZnO.

The strong fitting compliance assures the nature of these band gap emissions, with reduced electron-photon coupling at low temperatures defining clearer band edges that results in the characteristic blue shifts [27].

$$\text{Varshni relation}: E_{\mathrm{g}}(T) = E_{\mathrm{g}}(0) - \frac{\alpha T^2}{T+\beta},$$

where $E_{\mathrm{g}}(0)$ represents the material band gap at 0 K, and α and β are material-dependent phenomenological fitting constants. The experimentally fitted parameters (Figure S5) yield $E_{\mathrm{g}}(0)$ reasonably close to the inherent band gap for WS_2 at 2.0 eV, while α and β were obtained on the magnitude of 10^{-4} eV K^{-1} and 10^2 K, comparable to previously reported results for excitonic emissions in WS_2 monolayers [28–30].

To evaluate the effectiveness of the heterostructure at improving the trion-to-exciton ratio, a comparative study was made against a well-established factor – photodoping effects under laser power modulations [31–33]. As shown in Figure S6, the increment in measurement excitation power reflects obvious evolutions in peak intensity and peak shape for both the WS_2 on SiO_2 reference and WS_2 on ZnO heterostructure. Tabulated of the various peak intensities for comparison, a proportionate increase in the trion-to-exciton ratio metric was discernible, yielding an improvement of up to 2.506 times for WS_2 on SiO_2 when normalized against the lowest power measurement. Herein, it is imperative to note that the increase in excitation laser power by a factor of thousand presents a similar amplification factor in comparison to the formation of the heterostructure (2.21 times). The construction of the heterostructure thus eliminates the need for high laser power density during the measurement, assuring a lower possibility of sample damage. Nonetheless, the same metric for the WS_2 on the ZnO sample was able to achieve 4.615 times amplification at high excitation power, demonstrating the influence of the underlying ZnO layer, and prompting the potential for a compromise between trion enhancement and sample damage, to yield an optimal enhancement factor.

4 Conclusion

In this work, we have reported the formation of a WS_2-ZnO heterostructure that effectively boosts trion emission in the WS_2 component through efficient charge segregation at the type-II interface. The quantifier metric, I_{X^-}/I_{X^0}, was improved four-fold against a pristine WS_2 on SiO_2 reference, reaching a value of 2.21 that is comparable against that achievable through power-dependent photodoping. Simultaneously, the trion binding energy was strengthened under the influence of the underlying ZnO dielectric, reaching a heightened value of 59 meV. The capability to elevate trion composition with greater binding stability is expected to propel the development of optoelectronic nanodevices and future generation quantum photonics.

Acknowledgements This work was supported by NRF-NUS Resilience and Growth Postdoctoral Fellowship (Grant No. R-144-000-471-281).

Supporting information Table S1 and Figures S1–S6. The supporting information is available online at info.scichina.com and link.springer.com. The supporting materials are published as submitted, without typesetting or editing. The responsibility for scientific accuracy and content remains entirely with the authors.

References

1 Wang Y, Nie Z, Wang F. Modulation of photocarrier relaxation dynamics in two-dimensional semiconductors. Light Sci Appl, 2002, 9: 192
2 Huang L, Krasnok A, Alú A, et al. Enhanced light-matter interaction in two-dimensional transition metal dichalcogenides. Rep Prog Phys, 2022, 85: 046401
3 Lopez-Sanchez O, Lembke D, Kayci M, et al. Ultrasensitive photodetectors based on monolayer MoS_2. Nat Nanotech, 2013, 8: 497–501
4 Wang S, Wang J, Zhao W, et al. Efficient carrier-to-exciton conversion in field emission tunnel diodes based on MIS-type van der Waals heterostack. Nano Lett, 2017, 17: 5156–5162
5 Lei S, Wen F, Li B, et al. Optoelectronic memory using two-dimensional materials. Nano Lett, 2015, 15: 259–265
6 Ye Y, Xiao J, Wang H, et al. Electrical generation and control of the valley carriers in a monolayer transition metal dichalcogenide. Nat Nanotech, 2016, 11: 598–602
7 Miao S, Wang T, Huang X, et al. Strong interaction between interlayer excitons and correlated electrons in WSe_2/WS_2 moiré superlattice. Nat Commun, 2021, 12: 3608
8 Harankahage D, Cassidy J, Yang M, et al. Quantum computing with exciton qubits in colloidal semiconductor nanocrystals. J Phys Chem C, 2021, 125: 22195–22203
9 Ye Y, Wong Z J, Lu X, et al. Monolayer excitonic laser. Nat Photon, 2015, 9: 733–737
10 Chernikov A, Berkelbach T C, Hill H M, et al. Exciton binding energy and nonhydrogenic Rydberg series in monolayer WS_2. Phys Rev Lett, 2014, 113: 076802
11 Ugeda M M, Bradley A J, Shi S F, et al. Giant bandgap renormalization and excitonic effects in a monolayer transition metal dichalcogenide semiconductor. Nat Mater, 2014, 13: 1091–1095
12 Ye Z, Cao T, O'Brien K, et al. Probing excitonic dark states in single-layer tungsten disulphide. Nature, 2014, 513: 214–218
13 Sow B M, Lu J, Liu H, et al. Enriched fluorescence emission from WS_2 monoflake empowered by au nanoexplorers. Adv Opt Mater, 2017, 5: 1700156
14 Mak K F, He K, Lee C, et al. Tightly bound trions in monolayer MoS_2. Nat Mater, 2013, 12: 207–211
15 Riche F, Bragança H, Qu F, et al. Robust room temperature emissions of trion in darkish WSe_2 monolayers: effects of dark neutral and charged excitonic states. J Phys-Condens Matter, 2020, 32: 365702
16 Singh A, Moody G, Tran K, et al. Trion formation dynamics in monolayer transition metal dichalcogenides. Phys Rev B, 2016, 93: 041401
17 Boulesbaa A, Huang B, Wang K, et al. Observation of two distinct negative trions in tungsten disulfide monolayers. Phys Rev B, 2015, 92: 115443
18 Kesarwani R, Simbulan K B, Huang T D, et al. Control of trion-to-exciton conversion in monolayer WS_2 by orbital angular momentum of light. Sci Adv, 2022, 8: eabm0100
19 Chowdhury T, Paul D, Nechiyil D, et al. Modulation of trion and exciton formation in monolayer WS_2 by dielectric and substrate engineering. 2D Mater, 2021, 8: 045032
20 Wang S, Tian H, Ren C, et al. Electronic and optical properties of heterostructures based on transition metal dichalcogenides and graphene-like zinc oxide. Sci Rep, 2018, 8: 12009
21 Guan Y, Yao H, Zhan H, et al. Optoelectronic properties and strain regulation of the 2D WS_2/ZnO van der Waals heterostructure. RSC Adv, 2021, 11: 14085–14092
22 Golovynskyi S, Datsenko O I, Dong D, et al. Trion binding energy variation on photoluminescence excitation energy and power during direct to indirect bandgap crossover in monolayer and few-layer MoS_2. J Phys Chem C, 2021, 125: 17806–17819
23 Zhu B, Chen X, Cui X. Exciton binding energy of monolayer WS_2. Sci Rep, 2015, 5: 9218
24 Ross J S, Wu S, Yu H, et al. Electrical control of neutral and charged excitons in a monolayer semiconductor. Nat Commun, 2013, 4: 1474
25 Utama M I B, Kleemann H, Zhao W, et al. A dielectric-defined lateral heterojunction in a monolayer semiconductor. Nat Electron, 2019, 2: 60–65
26 Varshni Y P. Temperature dependence of the energy gap in semiconductors. Physica, 1967, 34: 149–154
27 Hu Z, Bao Y, Li Z, et al. Temperature dependent Raman and photoluminescence of vertical WS_2/MoS_2 monolayer heterostructures. Sci Bull, 2017, 62: 16–21
28 Koirala S, Mouri S, Miyauchi Y, et al. Homogeneous linewidth broadening and exciton dephasing mechanism in $MoTe_2$. Phys Rev B, 2016, 93: 075411
29 Yip C T, Lo T W, Zhu S C, et al. Tight-binding modeling of excitonic response in van der Waals stacked 2D semiconductors. Nanoscale Horiz, 2019, 4: 969–974
30 Plechinger G, Nagler P, Kraus J, et al. Identification of excitons, trions and biexcitons in single-layer WS_2. Phys Status Solidi RRL, 2015, 9: 457–461
31 Lundt N, Cherotchenko E, Iff O, et al. The interplay between excitons and trions in a monolayer of $MoSe_2$. Appl Phys Lett, 2018, 112: 031107
32 Zhang N, Surrente A, Baranowski M, et al. Impact of photodoping on inter- and intralayer exciton emission in a $MoS_2/MoSe_2/MoS_2$ heterostructure. Appl Phys Lett, 2018, 113: 062107
33 Yang Q, Xue Y, Chen H, et al. Photo-induced doping effect and dynamic process in monolayer $MoSe_2$. J Semicond, 2020, 41: 082004